Available online at website: https://jurnal.iaii.or.id/index.php/RESTI

JURNAL RESTI
(Rekayasa Sistem dan Teknologi Informasi)
Vol. 10 No. 1 (2026) 20 - 31 e-ISSN: 2580-0760

Comparative Analysis of Multispectral Image Classification Based on EfficientNetB0, ResNet152, DenseNet161, DenseNet121, and HSV Segmentation

Melinda Melinda[1*], Yudha Nurdin[2], Alfatirta Mufti[3], Syifa Anzella[4], Siti Rusdiana[5], Donata D. Acula[6]
[1,2,3,4]epartment of Electrical and Computer Engineering, Faculty of Engineering, Universitas Syiah Kuala, Banda Aceh, Indonesia
[5]Department of Mathematics, Faculty of Mathematics and Natural Sciences, Universitas Syiah Kuala, Banda Aceh, Indonesia
[6]Computer Science Department, University of Santo Tomas, Manila, Philippines

[1]melinda@usk.ac.id, [2]yudha.nurdin@usk.ac.id, [3]alfatirta.ee@usk.ac.id, [4]syifa.an@mhs.usk.ac.id, [5]siti.rusdiana@usk.ac.id, [6]ddacula@ust.edu.ph

Abstract

This study established a classification system based on Convolutional Neural Networks (CNNs) to detect High-High Fluctuation (HHF) patterns in multispectral data derived from pure water (H2O) and a water-sodium hydroxide (NaOH) solution. This study combines HSV color-space-based segmentation to identify areas with the highest signal amplitude, thereby enhancing the feature extraction of the CNN model. Data augmentation techniques, including random flipping, rotation, and color jitter, along with training parameters such as a learning rate of 0.0001 and a batch size of 32, have been shown to effectively improve model generalization and reduce overfitting. Four different CNN architectures were evaluated: ResNet-152, DenseNet-161, DenseNet-121, and EfficientNet-B0. As a result, ResNet152 achieved the highest accuracy of 97.6%, attributed to its network depth and residual connections that effectively address the vanishing gradient problem. DenseNet161 and DenseNet121 also demonstrated competitive performance, achieving accuracies of 96.7% and 96.2%, respectively, which is supported by their dense connectivity that optimizes feature reuse. Conversely, EfficientNetB0, despite showing lower accuracy (90%), provides significant computational efficiency, making it suitable for real-time applications. These results underscore the importance of selecting a CNN architecture that balances accuracy and efficiency for multispectral data classification.

Keywords: CNN; deep learning; HHF; HSV segmentation; multispectral data

How to Cite: [Melida, Y. Nurdin, A. Mufti, S. Anzella, S. Rusdiana, and D. D Acula, "Comparative Analysis of Multispectral Image Classification Based on EfficientNetB0, ResNet152, DenseNet161, DenseNet121, and HSV Segmentation", *J. RESTI (Rekayasa Sist. Teknol. Inf.)* , vol. 10, no. 1, pp. 20 - 31, Feb. 2026.
Permalink/DOI: https://doi.org/10.29207/resti.v10i1.6873

Received: June 30, 2025
Accepted: September 27, 2025
Available Online: February 16, 2026

This is an open-access article under the CC BY 4.0 License
Published by Ikatan Ahli Informatika Indonesia

1. Introduction

Multispectral signal processing has become an essential topic in various applications, particularly in the analysis of images generated when electromagnetic energy interacts with an object, reflecting or absorbing energy across the entire wavelength spectrum. This interaction produces signals consisting of various spectra, collectively called multispectral data [1]. Images generated from this data are called multispectral images, as they encompass more than one electromagnetic spectrum [2]. The main challenges encountered in multispectral signal processing are related to the signals themselves, specifically the instability of signal amplitudes caused by noise during data collection. These fluctuations in signal amplitude, caused by noise interference, can produce inconsistent data and make it difficult to identify relevant patterns in the signal [3], [4].

Previous research has demonstrated that image segmentation is crucial for identifying details in signal fluctuation patterns [5]. Segmentation distinguishes essential parts of an image based on specific characteristics, thereby facilitating the analysis and recognition of dominant features in fluctuation patterns. This study uses a threshold-based segmentation technique in the HSV (Hue, Saturation, Value) color space. HSV-based segmentation is considered adequate because it can isolate image segments based on color

components that are more representative than those of the RGB model [6].

This study uses data from previous research experiments involving two sample types: pure water (H2O) and a water-sodium hydroxide (NaOH) solution. The data was obtained using a Multispectral Capacitive Sensor (MSCS), which can capture capacitive signal variations at various wavelengths [7]. Through this acquisition process, we identified four distinct signal fluctuation patterns: High Mean Fluctuation (HMF), Mean Fluctuation (MF), High Fluctuation (HF), and High-High Fluctuation (HHF). Among these patterns, the HHF pattern was used in this analysis due to its striking signal amplitude contrast. Variations in HHF patterns pose a significant analytical challenge, as extraneous noise can lead to inaccuracies in their identification and classification. Therefore, the ability to recognize these patterns depends significantly on isolating areas with the highest signal amplitudes. Consequently, the primary issue addressed in this research is the management of signal amplitude variability induced by noise, as well as the improvement of accuracy in analyzing multispectral images affected by noise.

This study proposes using HSV color-space-based segmentation to address signal amplitude instability caused by noise. This method aims to isolate image segments with the highest signal amplitude in the HHF pattern [8]. By setting specific threshold values for each HSV component, this segmentation effectively separates areas with the highest signal amplitude in the multispectral image for each sample of H2O and H2O mixed with NaOH [9].

To classify segmented HHF fluctuation patterns, this study uses a Convolutional Neural Network (CNN) approach. CNN is known as one of the most widely used deep learning approaches and has demonstrated its effectiveness in various pattern recognition and image classification applications [10]. This network can automatically identify important features from images, thereby eliminating the need for manual feature extraction, making it highly suitable for complex pattern fluctuation classification tasks [9]. In this study, several CNN architectures known for their high performance in image classification tasks were employed, including EfficientNetB0, ResNet152, DenseNet161, and DenseNet121. Each architecture offers distinct advantages in terms of network depth, parameter efficiency, and generalization to new data.

EfficientNetB0 was chosen for its effective use of parameters and its ability to achieve high accuracy with relatively minimal computational resources [11]. ResNet152 also has the advantage of extracting deep features, specifically 152 layers, allowing for the extraction of intense and complex features [12]. DenseNet161 and DenseNet121 implement dense layer connectivity, meaning each layer gets inputs from all preceding layers [13]. This approach is beneficial in terms of feature reuse because it enhances the model's learning capabilities while minimizing the number of parameters required [14].

In previous research, HHF patterns were classified using the AlexNet CNN architecture, achieving 100% accuracy. However, the data used in previous research were limited to only 350 data points, which were primarily focused on HHF patterns in H2O [3].

This study, with its potential to revolutionize the field, not only builds and trains each CNN architecture but also evaluates the model's performance at distinguishing HHF patterns between H2O and H2O combined with NaOH.

Thus, this study contributes to the classification of HHF fluctuation patterns by improving the performance of image-based fluctuation pattern recognition systems through the use of advanced CNN architectures. In addition, HSV color space-based thresholding segmentation is employed to enhance the clarity of regions with the highest signal amplitude. Furthermore, this study provides a comparative analysis of HHF fluctuation pattern classification accuracy across several CNN architectures.

2. Methods

This section describes the methodology used in this study, including the characteristics of the multispectral fluctuation pattern data, the preprocessing and segmentation procedures, the CNN-based classification framework, and the evaluation metrics employed to assess model performance. An overview of the proposed classification workflow is illustrated in Figure 1.

2.1 Multispectral Image Dataset

This study uses H2O data and H2O mixed with NaOH obtained from previous research [7]. The data was obtained from the data acquisition process using a Multispectral Capacitive Sensor (MSCS). As a result, there are four types of fluctuation patterns: High Mean Fluctuation (HMF), Mean Fluctuation (MF), High Fluctuation (HF), and High-High Fluctuation (HHF) in the form of a matrix with dimensions of 8193 x 91. We then converted the matrix data into a two-dimensional image.

In this study, we used the High-High Fluctuation (HHF) pattern image because it produced the most contrasting fluctuation pattern based on signal amplitude. The HHF fluctuation pattern image data consisted of 1,050 data points, comprising 525 H2O data images and 525 H2O data images mixed with NaOH. Figure 2 shows an example of H2O and H2O mixed with NaOH signals based on the High-High Fluctuation (HHF) pattern. This figure shows a clear difference in fluctuation amplitude between H2O and H2O mixed with NaOH.

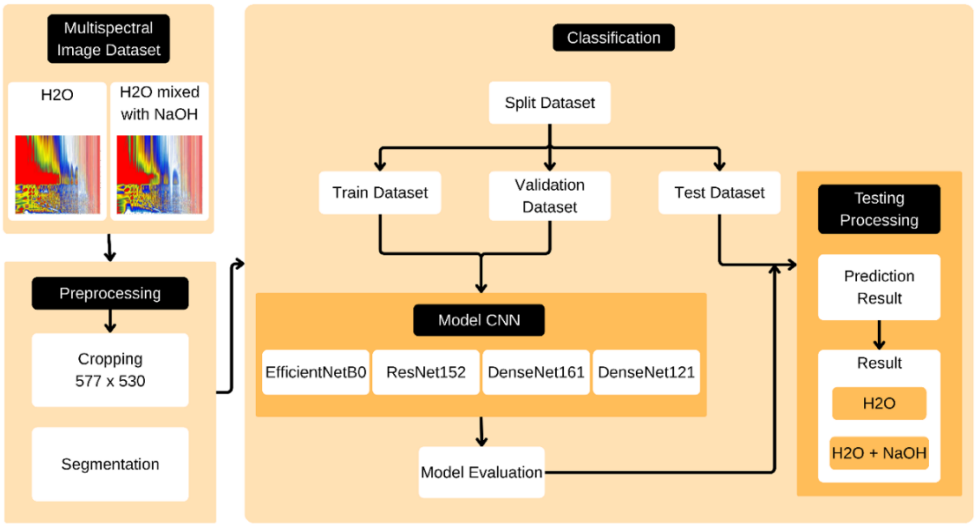
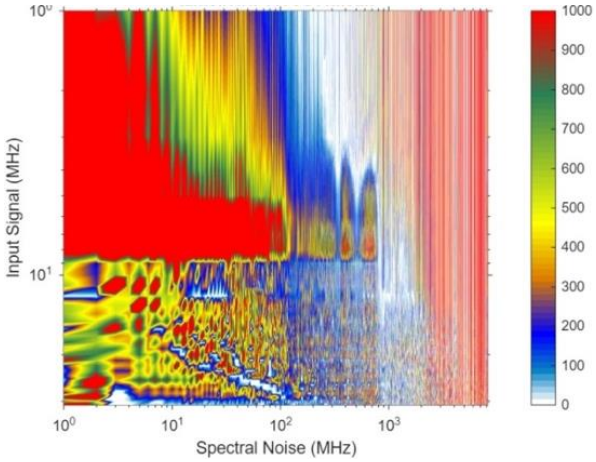
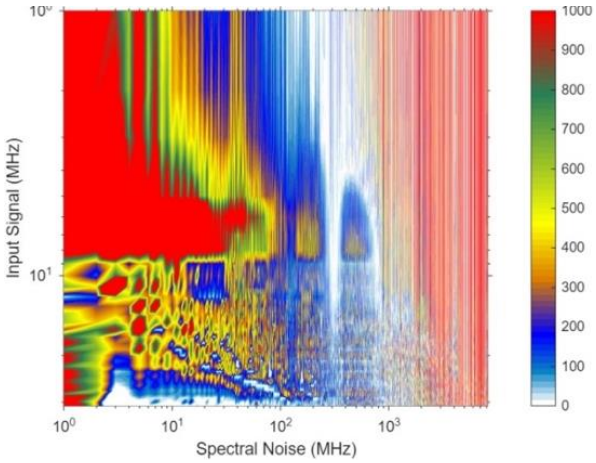


Figure 1. Overall workflow of HHF fluctuation pattern classification for H2O and H2O mixed with NaOH.



(a)



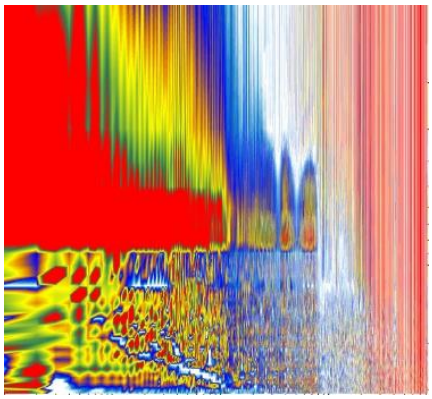
(b)

Figure 2. Fluctuation pattern of HHF: (a) H2O, (b) H2O with NaOH.

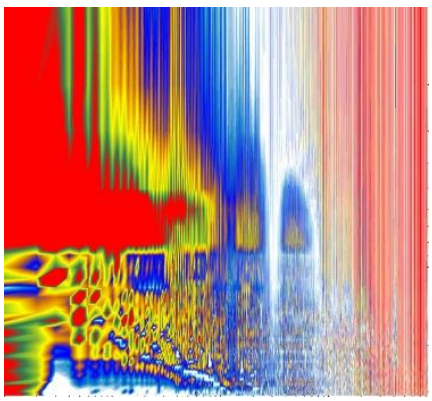
2.2 Preprocessing and Segmentation

This subsection explains the preprocessing steps applied to the HHF fluctuation pattern images prior to classification. The segmentation process is designed to isolate regions with the highest signal amplitude using HSV color-space-based thresholding.

Image cropping was first applied to focus the analysis on the region of interest containing the HHF fluctuation pattern. Cropping is commonly used to remove irrelevant image areas and reduce computational complexity [15]. In this study, the HHF images for both H_2O and H_2O mixed with NaOH were cropped to a resolution of 577 × 530 pixels, ensuring that only the dominant fluctuation regions were retained for further processing. Figure 3 illustrates the cropped HHF images for both samples.



(a)



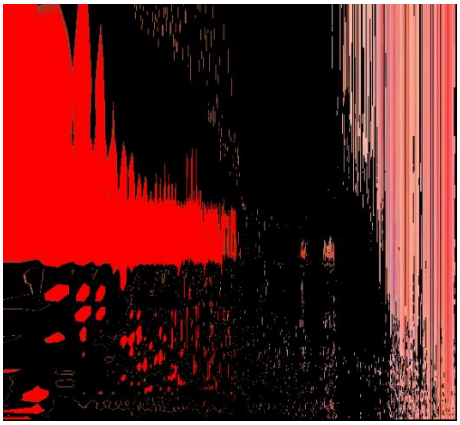
(b)

Figure 3. Cropping results of the HHF fluctuation pattern image: (a) H2O, (b) H2O mixed with NaOH.

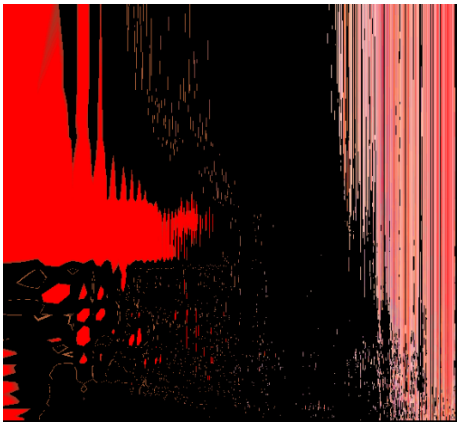
After cropping, HSV color-space-based thresholding segmentation was applied to isolate the highest-amplitude regions in the HHF images. The HSV color space was selected because it provides a clearer separation of color intensity information compared to the RGB model and allows effective identification of amplitude-dominant regions under varying illumination conditions [16], [17]. In the converted HHF images, the highest signal amplitudes are visually represented by red-dominant regions.

Segmentation was performed by converting the cropped images from RGB to HSV and applying experimentally determined threshold values. The hue component was restricted to two intervals corresponding to red color intensity, namely 0–10° and 160–180°, while the saturation and value components were set to 50–255 and 150–255, respectively. These thresholds were chosen to retain pixels associated with high-amplitude HHF responses while suppressing background and low-amplitude regions.

The resulting binary masks effectively highlight regions with the strongest signal amplitudes in both H_2O and H_2O mixed with NaOH samples. The segmented HHF fluctuation patterns are presented in Figure 4, demonstrating clear separation between the high-amplitude regions and the background.



(a)



(b)

Figure 4. HSV segmentation results on HHF fluctuation pattern images: (a) H2O, (b) H2O mixed with NaOH.

2.3 Dataset Preparation and Augmentation

This study uses 1,050 HHF fluctuation pattern image data, comprising 525 H2O images and 525 H2O images mixed with NaOH. Each dataset is divided into three parts, namely train, validation, and test, with a ratio of 64%: 16%: 20%. This ratio was chosen to optimize the use of training data without compromising the quality of validation and test data [18].

Data augmentation was performed on the training data to improve the performance of the CNN model [19]. Augmentation was performed by resizing the images to $224x224$ pixels and applying transformations such as random horizontal and vertical flips, random rotations up to 30 degrees, random resized crops, and affine transformations to enrich data variation and prevent overfitting. Color jitter is used to improve the model's robustness against variations in lighting and color. Images are converted to tensors and normalized using the dataset's mean and standard deviation. This combination of techniques has been proven to improve model accuracy and generalization while preventing overfitting [20].

2.4 CNN-Based Classification

This subsection describes the CNN-based classification procedure used to distinguish HHF fluctuation patterns of H_2O and H_2O mixed with NaOH. The classification process consists of model training and testing stages, following the workflow illustrated in Figure 1. During training, labeled HHF images were used to learn discriminative features, while during testing, unseen images were employed to evaluate the generalization capability of the trained models.

All CNN models were trained using the same dataset split and preprocessing pipeline to ensure a fair comparison. The Adam optimizer was employed with a learning rate of 0.0001 and a batch size of 32. Training was conducted for 40 epochs, providing sufficient iterations for convergence while minimizing the risk of overfitting. These training parameters were consistently applied across all architectures to allow performance differences to be attributed primarily to architectural characteristics rather than optimization settings.

To investigate the impact of network architecture on HHF fluctuation pattern classification, four state-of-the-art CNN models were selected: EfficientNetB0, ResNet152, DenseNet161, and DenseNet121. These architectures were chosen to represent different design philosophies, including parameter-efficient scaling, deep residual learning, and dense feature reuse.

EfficientNetB0 was employed in this study as a parameter-efficient CNN architecture to evaluate its capability in classifying HHF fluctuation patterns. The model adopts a compound scaling strategy that jointly optimizes network depth, width, and input resolution, enabling effective feature extraction with a relatively small number of parameters [21]. EfficientNetB0 consists of an initial convolutional layer followed by a

sequence of Mobile Inverted Bottleneck Convolution (MBConv) blocks integrated with squeeze-and-excitation mechanisms to enhance feature representation.

In the context of this study, EfficientNetB0 serves as a lightweight baseline for assessing whether compact architectures can capture discriminative features from segmented HHF images. Feature extraction is followed by global average pooling to reduce spatial dimensionality, and classification is performed using a fully connected output layer [22]. The overall architecture of EfficientNetB0 is illustrated in Figure 5. Previous studies have demonstrated the competitive performance of EfficientNetB0 in image classification tasks, including skin disease classification [23] and plant classification [24].

ResNet152 was selected to investigate the effect of deep residual learning on HHF fluctuation pattern classification. This architecture comprises 152 convolutional layers organized into residual blocks, which employ shortcut connections to facilitate gradient flow and enable effective training of deep networks [25]. Such depth allows the extraction of complex and hierarchical features from input images.

In this study, ResNet152 was used to assess whether deeper feature representations improve the discrimination of HHF patterns between H_2O and H_2O mixed with NaOH. After feature extraction through residual blocks, global average pooling and a fully connected layer are applied to generate classification outputs [26]. The architecture of ResNet152 is presented in Figure 6. ResNet152 has been successfully applied in various classification domains, including lung cancer classification [27] and audio spoofing detection [28].

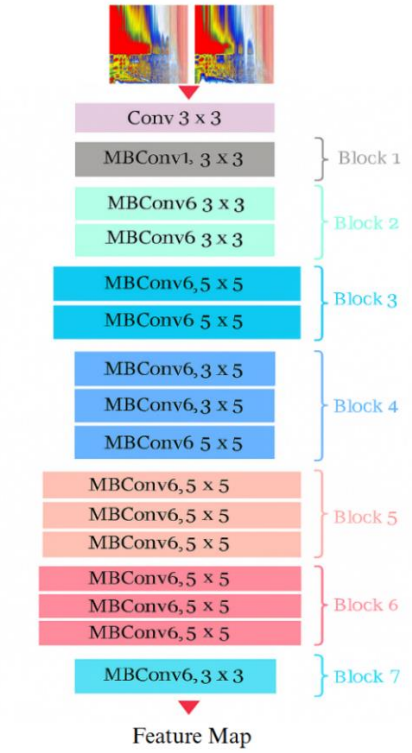


Figure 5. Illustration of the architecture of EfficientNetB0

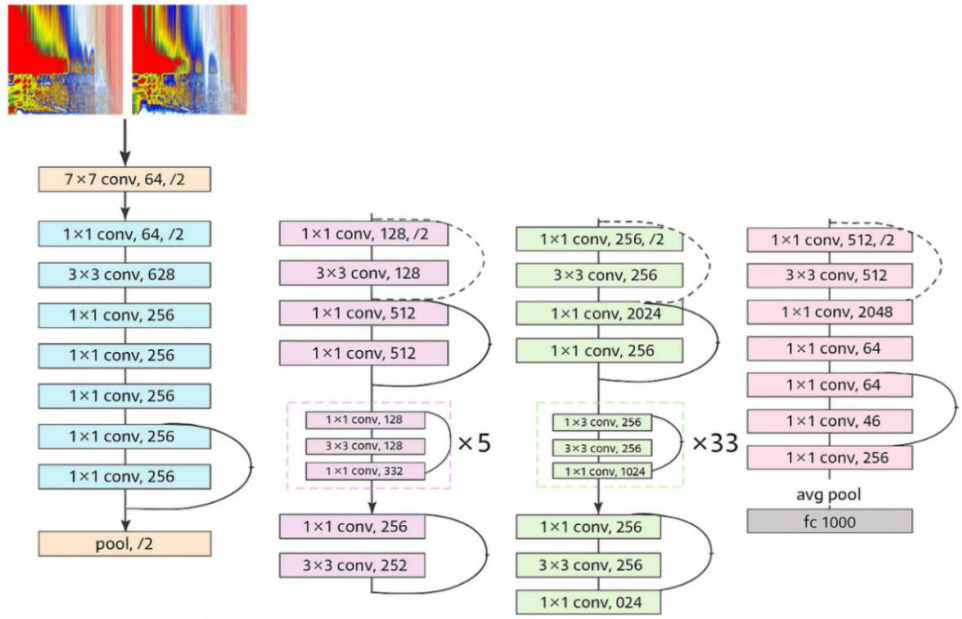


Figure 6. Illustration of the architecture of ResNet152

DenseNet161 was employed to examine the influence of dense feature reuse on the classification of HHF fluctuation patterns. This architecture implements dense connectivity, where each layer receives feature maps from all preceding layers, promoting efficient information flow and gradient propagation [29]. DenseNet161 consists of 161 convolutional layers arranged into multiple dense blocks separated by transition layers.

Within this study, DenseNet161 enables comprehensive feature aggregation across layers, which is beneficial for capturing subtle amplitude variations in segmented

HHF images. Batch normalization and ReLU activation are applied prior to convolutional operations to stabilize training. The classification output is produced after global average pooling and a fully connected layer [30]. The architecture of DenseNet161 is illustrated in Figure 7. DenseNet161 has been applied in several prior studies, including pancreatic cystic tumor classification [31] and vein pattern recognition [32].

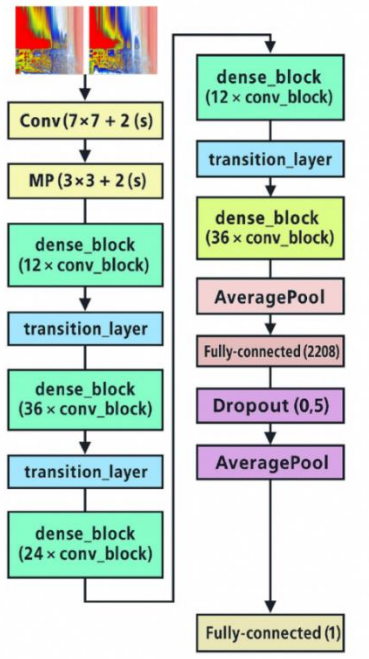


Figure 7. Illustration of the architecture of DenseNet161

DenseNet121 was included as a more compact alternative within the DenseNet family to evaluate the trade-off between classification performance and computational efficiency. This architecture consists of 121 convolutional layers arranged in a dense connectivity framework similar to DenseNet161, but with fewer parameters [13].

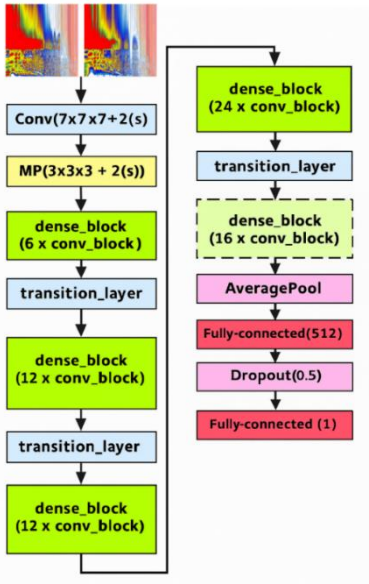


Figure 8. Illustration of the architecture of DenseNet121

In this study, DenseNet121 was used to determine whether a lighter dense architecture can effectively classify HHF fluctuation patterns while reducing computational cost. The model applies batch normalization and ReLU pre-activation before convolutional layers, followed by dense feature extraction, spatial dimensionality reduction through pooling, and global average pooling. Classification is completed using a fully connected output layer [33]. The architecture of DenseNet121 is shown in Figure 8. Previous studies have reported strong performance of DenseNet121 in image classification tasks, such as weather classification [34] and tomato leaf disease detection [35].

2.5 Evaluation

The performance of the proposed CNN-based classification models was evaluated to assess their ability to distinguish between H_2O and H_2O mixed with NaOH based on HHF fluctuation pattern images. After the training process was completed, the best-performing model from each CNN architecture was selected and applied to the test dataset, which was not involved in the training or validation stages. Model predictions were compared with ground truth labels to quantify classification performance. Several evaluation metrics commonly used in binary classification were employed, including accuracy, precision, recall, and F1-score, which are mathematically defined in Equations 1-4.

$$\text{Accuracy} = \frac{(\text{TP} + \text{TN})}{(\text{TP} + \text{FP} + \text{TN} + \text{FN})} \quad (1)$$

$$\text{Precision} = \frac{(\text{TP})}{(\text{TP} + \text{FP})} \quad (2)$$

$$\text{Recall} = \frac{(\text{TP})}{(\text{TP} + \text{FN})} \quad (3)$$

$$\text{F1 - Score} = 2 \times \frac{(\text{Recall} \times \text{Precision})}{(\text{Recall} \times \text{Precision})} \quad (4)$$

In these equations, TP (true positive) denotes the number of H_2O samples correctly classified as H_2O, TN (true negative) represents the number of H_2O mixed with NaOH samples correctly classified as H_2O mixed with NaOH, FP (false positive) indicates the number of H_2O mixed with NaOH samples incorrectly classified as H_2O, and FN (false negative) refers to the number of H_2O samples incorrectly classified as H_2O mixed with NaOH.

In addition to these metrics, the Receiver Operating Characteristic (ROC) curve and the Area Under the Curve (AUC) were used to evaluate the discriminative capability of each model. The ROC curve illustrates the relationship between the true positive rate (TPR) and the false positive rate (FPR) across different classification thresholds, where $TPR = TP / (TP + FN)$ and $FPR = FP / (FP + TN)$. ROC–AUC analysis provides insight into the trade-off between sensitivity and specificity and is widely used to assess binary classification performance [34-36].

To statistically analyze performance differences among the evaluated CNN architectures, one-way Analysis of Variance (ANOVA) was applied to the classification accuracy results. ANOVA was employed to determine whether the observed differences in accuracy among EfficientNetB0, ResNet152, DenseNet161, and DenseNet121 were statistically significant [37], [38]. A significance level of 0.05 was adopted; a p-value below this threshold indicates a significant difference in model performance, whereas a p-value greater than or equal to 0.05 suggests that performance differences are not statistically significant [39], [40]. This analysis enables objective comparison of the CNN architectures and supports the identification of the most effective model for HHF fluctuation pattern classification [41].

3. Results and Discussions

3.1 Multispectral Dataset

This study utilizes High-High Fluctuation (HHF) H2O and H2O mixed with NaOH data, obtained from previous research, in the form of a matrix with a size of 8193 x 91 [7]. The matrix data was then converted into a 2-dimensional image. A total of 1,050 HHF fluctuation pattern images were obtained, consisting of 525 H2O data images and 525 H2O mixed with NaOH data images. All images underwent cropping and threshold-based segmentation in the HSV color space, enabling effective identification of areas with the highest amplitude values.

Each dataset is divided into three parts: training, validation, and testing, with ratios of 64%:16%:20 %, respectively. Data augmentation was applied to the training data to enhance the performance of the CNN model. Augmentation was performed by resizing the images to $224x224$ pixels and applying transformations such as random horizontal and vertical flips, random rotations up to 30 degrees, random resized crops, and affine transformations to enrich data variation and prevent overfitting. Color jitter was used to enhance the model's robustness to lighting and color variations. Then, these image data were used as input to four CNN architectures in this study, each trained separately to classify solutions based on patterns observed after segmentation. The combination of focused segmentation with efficient CNN architectures is expected to improve classification accuracy for subtle spectral changes between classes.

3.2 Training Result and Dataset Validation

During the training phase, the model was trained for 50 epochs on the training data. Each CNN model with the highest validation accuracy and the lowest validation loss was used to evaluate its performance in detecting HHF H2O and H2O mixed with NaOH fluctuation patterns. The EfficientNetB0 model achieved the best validation loss value at epoch 47. At that epoch, the training accuracy was 87.5%, the validation accuracy was 95.8%, and the validation loss was 0.144. Figure 9 compares training and validation accuracy, along with graphs of the training and validation losses.

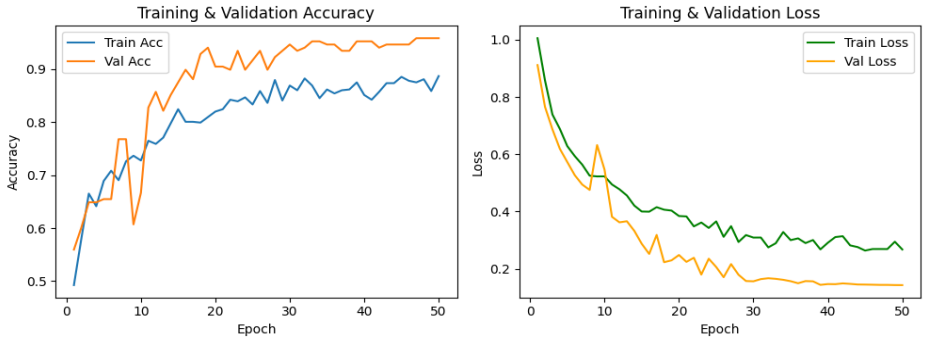


Figure 9. Epoch results using EfficientNetB0 architecture

In the ResNet152 model, the best validation loss value was achieved at epoch 29, with a validation loss of 0.056 after 50 epochs. At that epoch, the training accuracy was 92.3%, and the validation accuracy was 98.2%. Figure 10 shows a graph comparing training and validation accuracy, along with another graph comparing training and validation loss.

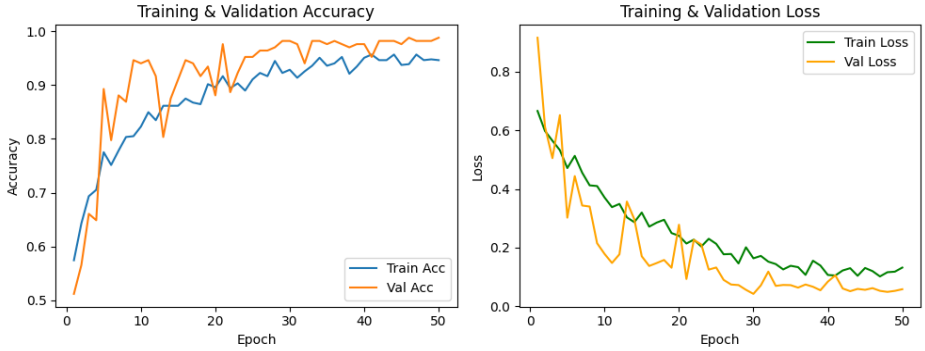


Figure 10. Epoch results using ResNet152 architecture.

In the constructed DenseNet161 model, the best validation loss value was achieved at epoch 35. At that epoch, the training accuracy was 94.5%, the validation accuracy was 98.8%, and the validation loss was 0.068. The graphs comparing training and validation accuracy, as well as those showing training and validation loss for DenseNet161, are shown in Figure 11.

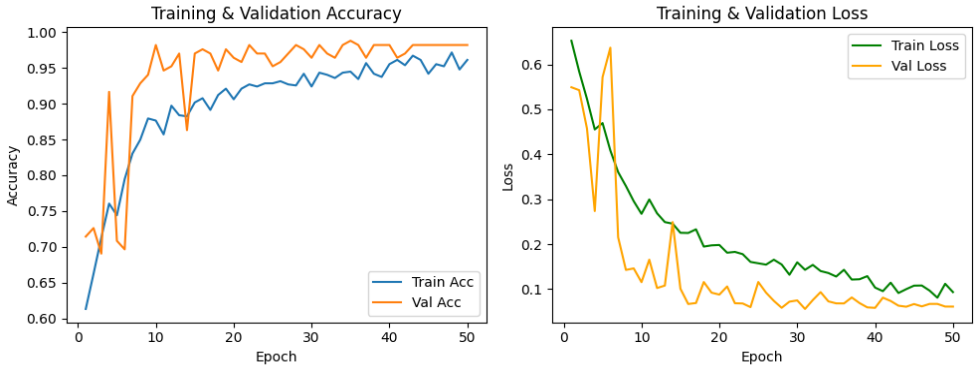


Figure 11. Epoch results using DenseNet161 architecture.

In the DenseNet121 model, the best validation loss value was achieved at epoch 28, with a validation loss of 0.060 after 50 epochs. At that epoch, the training accuracy was 89.4%, and the validation accuracy was 97.6%. Figure 12 compares training and validation accuracy and shows training and validation loss for DenseNet-121.

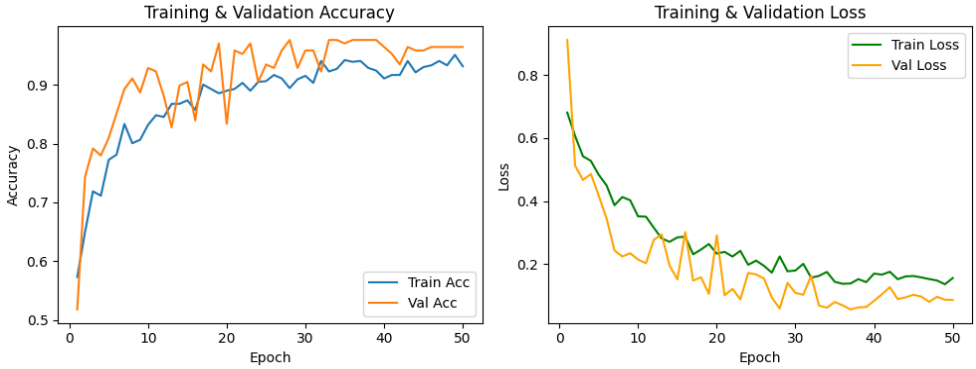


Figure 12. Epoch results using DenseNet121 architecture.

3.3 Testing Result

During the testing phase, the dataset consisted of 210 HHF fluctuation pattern images, comprising 105 H2O images and 105 H2O images mixed with NaOH. The testing data were not involved in the training or validation processes and were used exclusively to evaluate the generalization capability of the trained CNN models.

Figures 13–16 present the confusion matrices obtained from the testing results of each CNN architecture. These confusion matrices provide a detailed representation of classification outcomes, including TP, FP, TN, and FN predictions for each model.

Figure 13 shows the confusion matrix for the EfficientNetB0 model, which correctly classified 99 H2O images as TP and 96 H2O mixed with NaOH images as TN. However, 6 H2O images were misclassified as H2O mixed with NaOH (FN), and 9 H_2O mixed with NaOH images were misclassified as H_2O (FP).

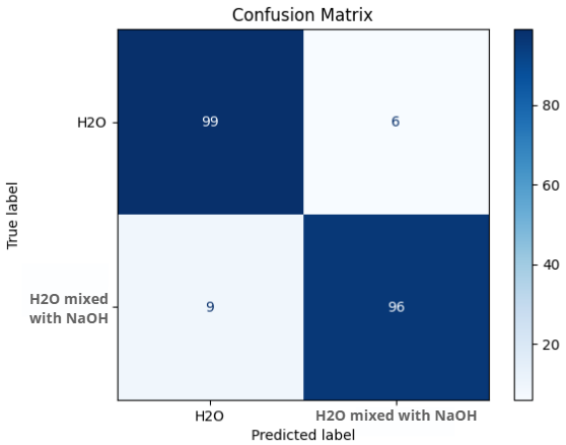


Figure 13. Confusion matrix EfficientNetB0.

Figure 14 illustrates the confusion matrix of the ResNet152 model. This model correctly identified 102 H2O images (TP) and 101 H2O mixed with NaOH images (TN), with only 3 FN and 4 FP, indicating a strong classification performance.

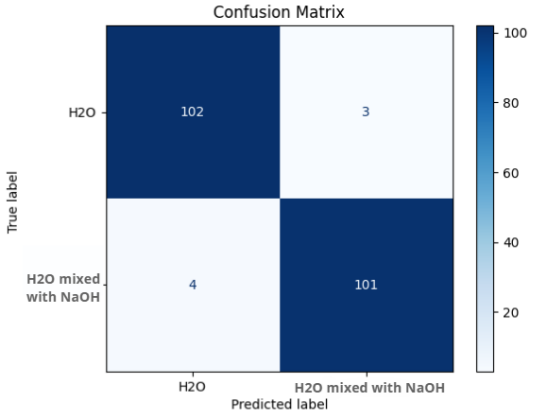


Figure 14. Confusion matrix ResNet152.

Figure 15 presents the confusion matrix results for the DenseNet161 model. The model achieved 100 TP classifications and 103 TN classifications, while producing 5 FN and only 2 FP, demonstrating highly accurate discrimination between the two classes.

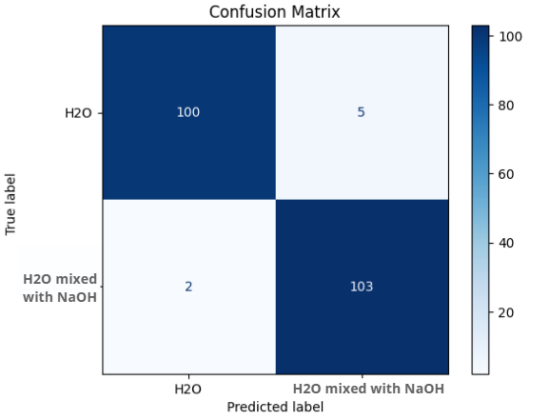


Figure 15. Confusion matrix DenseNet161.

Figure 16 shows the confusion matrix of the DenseNet121 model, which correctly classified 98 H_2O images (TP) and 102 H_2O mixed with NaOH images (TN). Meanwhile, 7 false negatives (FN) and 3 false positives (FP) were observed.

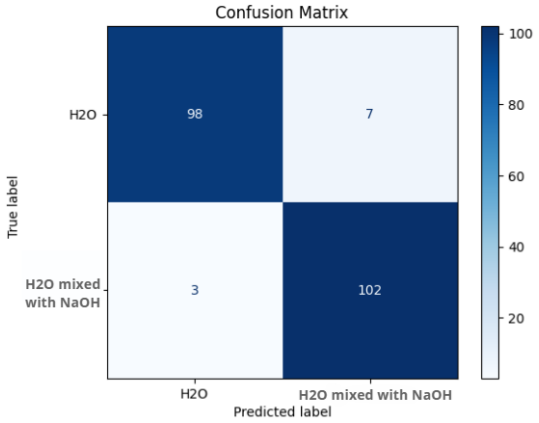


Figure 16. Confusion matrix DenseNet121.

Based on the confusion matrices presented in Figures 13–16, quantitative performance metrics, including accuracy, precision, recall, and F1-score, were calculated for each CNN model. The resulting evaluation metrics are summarized in Table 1.

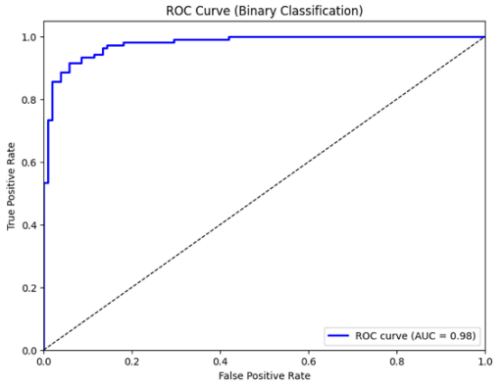
Table 1. Results of evaluation metric calculations

Model	Accuracy	Precision	Recall	F1-score
EfficientNetB0	93%	93%	93%	93%
ResNet152	97%	97%	97%	97%
DenseNet161	97%	97%	97%	97%
DenseNet121	95%	95%	95%	95%

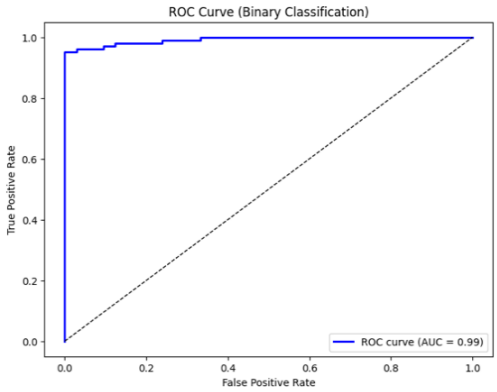
As shown in Table 1, EfficientNetB0 achieved the lowest overall performance, with accuracy, precision, recall, and F1-score values of 93%. This result indicates limitations in capturing discriminative HHF fluctuation features when compared to deeper architectures. In contrast, ResNet152 and DenseNet161 demonstrated superior and consistent performance, achieving accuracies of 97%. The strong performance of ResNet152 can be attributed to its deep residual architecture, which facilitates effective extraction of complex features. DenseNet161, despite having a more compact structure than ResNet152, achieved comparable accuracy due to its dense connectivity, which promotes efficient feature reuse and gradient propagation. DenseNet121 also delivered strong performance with an accuracy of 95%, indicating its suitability for complex fluctuation pattern recognition with reduced computational complexity.

While confusion matrices and evaluation metrics provide threshold-dependent performance measures, further analysis was conducted using Receiver Operating Characteristic (ROC) curves and Area Under the Curve (AUC) values to assess the discriminative capability of each model across varying classification thresholds. The ROC curves for all CNN architectures are presented in Figure 17, and the corresponding AUC values are summarized in Figure 18.

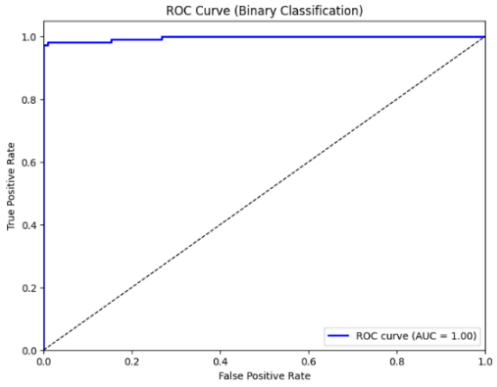
The ROC–AUC analysis indicates that the ResNet152 model achieved an AUC value of 0.99, demonstrating excellent class separability. DenseNet161 achieved a perfect AUC of 1.00, indicating flawless discrimination between H_2O and H_2O mixed with NaOH across all threshold values. DenseNet121 also showed strong performance with an AUC of 0.99, closely matching ResNet152. Although EfficientNetB0 yielded a slightly lower AUC value of 0.98, the result still reflects a high discriminative capability, particularly considering its lightweight architecture. To statistically evaluate whether the observed differences in classification accuracy among the CNN models were significant, one-way ANOVA was applied. The analysis produced an F-statistic of 20.497 with a p-value of 0.001, indicating a statistically significant difference in accuracy across EfficientNetB0, ResNet152, DenseNet161, and DenseNet121. The low p-value confirms that the observed performance differences are unlikely to be caused by random variation and highlights the importance of selecting an appropriate CNN architecture for HHF fluctuation pattern classification.



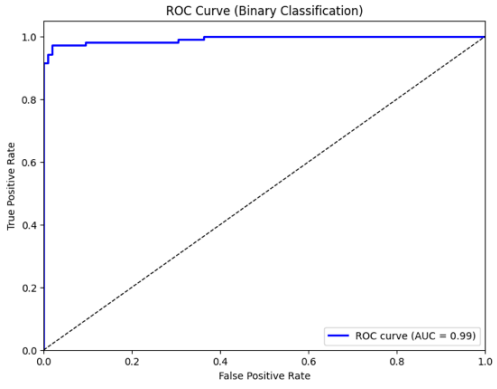
(a)



(b)



(c)



(d)

Figure 17. ROC graph results for the models: (a) EfficientNetB0; (b) Resnet152; (c) DenseNet161; (d) DenseNet121

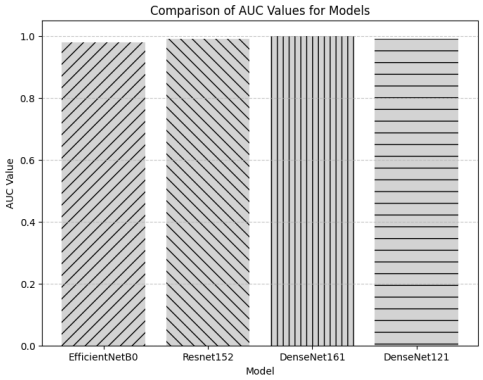


Figure 18. Comparison of AUC values for each model.

Compared with previous studies that employed the AlexNet architecture and achieved 100% accuracy using a smaller dataset of 350 HHF samples focused solely on H_2O [3], the present study demonstrates that deeper and more advanced CNN architectures—particularly ResNet152 and DenseNet161—exhibit robust performance when applied to larger and noisier multispectral datasets involving both H_2O and H_2O mixed with NaOH. Although the achieved accuracy ranges from 95% to 97%, the results indicate improved generalization and resilience to noise, underscoring the critical role of architectural selection in multispectral image classification tasks.

4. Conclusions

This study focuses on developing a Convolutional Neural Network (CNN)-based classification system to identify High-High Fluctuation (HHF) patterns in multispectral data generated from pure water (H2O) and water solutions containing sodium hydroxide (NaOH). Test results show that combining HSV color-space-based segmentation with an advanced CNN architecture achieves high classification accuracy. HSV segmentation has proven effective at isolating areas with the highest signal amplitude, thereby facilitating the model's feature extraction. Data augmentation processes, including random flip, rotation, and color jitter, as well as training parameters such as a learning rate of 0.0001 and a batch size of 32, play a crucial role in enhancing model generalization and preventing overfitting.

The results from the four CNN architectures tested show that ResNet152 and DenseNet161 achieve 97% accuracy. This is attributed to ResNet152's network depth and residual connection mechanism, which addresses the vanishing gradient problem. Additionally, DenseNet161's dense connectivity design enables optimal feature reuse. Although DenseNet161 is more compact than ResNet152, it still delivers excellent results recognizing complex fluctuation patterns thanks to its ability to accelerate information flow and gradient updates through dense layer connectivity. Meanwhile, DenseNet121 achieved 95% accuracy, and EfficientNetB0 had lower accuracy (93%), despite its superior computational efficiency and suitability for

real-time applications.

The ANOVA results indicate a significant difference in accuracy among the CNN models, with a very small p-value (0.001), confirming the importance of selecting the appropriate model for classification. Although EfficientNetB0 is more computationally efficient, ResNet152 and DenseNet161 achieve superior classification accuracy.

These results suggest that we tailor the selection of CNN architectures to strike a balance between accuracy and efficiency. In the future, further research is expected to explore ensemble learning techniques or attention mechanisms to improve accuracy and to test models on larger, more diverse datasets.

Acknowledgements

We would like to thank the LPPM of Universitas Syiah Kuala for funding this research through a Lecturer Research Grant with number 172/UN11/SPK/PNBP/2021.

References

[1] O. Gutierrez-Navarro, L. Granados-Castro, A. R. Mejia-Rodriguez, and D. U. Campos-Delgado, "A Multi-Spectral Image Database for In-Vivo Hand Perfusion Evaluation," *IEEE Access*, vol. 11, no. July, pp. 87543–87557, 2023, doi: 10.1109/ACCESS.2023.3305256.

[2] B. Rusyn, O. Lutsyk, R. Kosarevych, T. Maksymyuk, and J. Gazda, "Features extraction from multi-spectral remote sensing images based on multi-threshold binarization," *Sci. Rep.*, 2023, doi: 10.1038/s41598-023-46785-7.

[3] M. Melinda, Y. Yunidar, and N. A. C. Andryani, "Application of Convolutional Neural Network (CNN) Method in Fluctuations Pattern," *Green Intell. Syst. Appl.*, vol. 3, no. 2, pp. 56–68, 2023, doi: 10.53623/gisa.v3i2.270.

[4] J. J. Senecal, J. W. Sheppard, and J. A. Shaw, "Efficient Convolutional Neural Networks for Multi-Spectral Image Classification," in *Proceedings of the International Joint Conference on Neural Networks*, 2019. doi: 10.1109/IJCNN.2019.8851840.

[5] Melinda, A. S. Tamsir, D. Sudiana, D. Gunawan, and M. Iqbal, "Implementation of segmentation scheme based on wavelet transform in multi-spectral fluctuation patterns," *J. Telecommun. Electron. Comput. Eng.*, vol. 8, no. 12, pp. 47–52, 2016, https://jtec.utem.edu.my/jtec/article/view/1434

[6] D. Giuliani, "Metaheuristic Algorithms Applied to Color Image Segmentation on HSV Space," *J. Imaging*, vol. 8, no. 1, 2022, doi: 10.3390/jimaging8010006.

[7] M. Melinda, A. Tanjung, A. S. Tamsir, B. Basari, and D. Gunawan, "Grouped data analysis of H2O and H2O mixed with NaOH on multi spectral high fluctuation pattern," *Proc. - 2017 Int. Conf. Electr. Eng. Informatics Adv. Knowledge, Res. Technol. Humanit. ICELTICs 2017*, vol. 2018-Janua, no. ICELTICs, pp. 184–188, 2017, doi: 10.1109/ICELTICS.2017.8253266.

[8] S. Ortega, M. Halicek, H. Fabelo, G. M. Callico, and B. Fei, "Hyperspectral and multispectral imaging in digital and computational pathology: a systematic review [Invited]," *Biomed. Opt. Express*, 2020, doi: 10.1364/boe.386338.

[9] G. B. Satrya, I. N. A. Ramatryana, and S. Y. Shin, "Compressive Sensing of Medical Images Based on HSV Color Space," *Sensors*, 2023, doi: 10.3390/s23052616.

[10] Y. Yunidar, Y. Yusni, N. Nasaruddin, and F. Arnia, "CNN Performance Improvement for Classifying Stunted Facial Images Using Early Stopping Approach," *J. RESTI*, vol. 9, no. 1, pp. 62–68, 2025, doi: 10.29207/resti.v9i1.6068.

[11] A. El Bergui, A. Porebski, and N. Vandenbroucke, "A lightweight spatial and spectral CNN model for classifying floating marine plastic debris using hyperspectral images," *Mar. Pollut. Bull.*, vol. 216, no. December 2024, p. 117965, 2025, doi: 10.1016/j.marpolbul.2025.117965.

[12] A. Dastgir, W. Bin, M. U. Saeed, J. Sheng, L. Site, and H. Hassan, "Attention LinkNet-152: a novel encoder-decoder based deep learning network for automated spine segmentation," *Sci. Rep.*, vol. 15, no. 1, pp. 1–13, 2025, doi: 10.1038/s41598-025-95243-z.

[13] N. Hasan, Y. Bao, A. Shawon, and Y. Huang, "DenseNet Convolutional Neural Networks Application for Predicting COVID-19 Using CT Image," *SN Comput. Sci.*, vol. 2, no. 5, pp. 1–11, 2021, doi: 10.1007/s42979-021-00782-7.

[14] T. Chauhan, H. Palivela, and S. Tiwari, "Optimization and fine-tuning of DenseNet model for classification of COVID-19 cases in medical imaging," *Int. J. Inf. Manag. Data Insights*, vol. 1, no. 2, p. 100020, 2021, doi: 10.1016/j.jjimei.2021.100020.

[15] S. H. Lee *et al.*, "Cropper : Vision-Language Model for Image Cropping through In-Context Learning", DOI: https://doi.org/10.48550/arXiv.2408.07790

[16] L. He, X. Cheng, A. Jiwa, D. Li, J. Fang, and Z. Du, "Zanthoxylum bungeanum Fruit Detection by Adaptive Thresholds in HSV Space for an Automatic Picking System," *IEEE Sens. J.*, vol. 23, no. 13, pp. 14471–14486, 2023, doi: 10.1109/JSEN.2023.3277042.

[17] S. S. Sitanggang, Y. Yuhandri, and Adil Setiawan, "Image Transformation With Lung Image Thresholding and Segmentation Method," *J. RESTI (Rekayasa Sist. dan Teknol. Informasi)*, vol. 7, no. 2, pp. 278–285, 2023, doi: 10.29207/resti.v7i2.4321.

[18] V. R. Joseph, "Optimal ratio for data splitting," *Stat. Anal. Data Min.*, vol. 15, no. 4, pp. 531–538, 2022, doi: 10.1002/sam.11583.

[19] W. Zeng, "Image data augmentation techniques based on deep learning: A survey," *Math. Biosci. Eng.*, vol. 21, no. 6, pp. 6190–6224, 2024, doi: 10.3934/mbe.2024272.

[20] S. Kumar, P. Asiamah, O. Jolaoso, and U. Esiowu, "Enhancing Image Classification with Augmentation: Data Augmentation Techniques for Improved Image Classification," 2025, [Online]. Available: http://arxiv.org/abs/2502.18691

[21] V. T. Hoang and K. H. Jo, "Practical Analysis on Architecture of EfficientNet," *Int. Conf. Hum. Syst. Interact. HSI*, vol. 2021-July, pp. 2–5, 2021, doi: 10.1109/HSI52170.2021.9538782.

[22] P. Jyothi, D. Haritha, and K. Arava, "Gender Classification Using Efficientnetb0 And Mobilenetv2," vol. 14, no. 27, pp. 694–700, 2025, https://www.jneonatalsurg.com/index.php/jns/article/view/6499

[23] P. Khairunnisa, W. E. Putra, and W. Yitong, "Convolutional Neural Networks Using EfficientNetB0 Architecture and Hyperparameters on Skin Disease Classification," vol. 2, no. January, pp. 127–137, 2025, DOI: https://doi.org/10.57152/predatecs.v2i2.1569

[24] N. P. Maylianti, I. G. Ngurah, L. Wijayakusuma, I. P. Chandra, and A. Wiguna, "Comparison of EfficientNet-B0 and ResNet-50 for Detecting Diseases in Cocoa Fruit," vol. 9, no. 1, pp. 115–120, 2025, DOI: https://doi.org/10.30871/jaic.v9i1.8868

[25] S. A. Hasanah, A. A. Pravitasari, A. S. Abdullah, I. N. Yulita, and M. H. Asnawi, "A Deep Learning Review of ResNet Architecture for Lung Disease Identification in CXR Image," *Appl. Sci.*, vol. 13, no. 24, 2023, doi: 10.3390/app132413111.

[26] W. Xu and R. S. Cloutier, "A facial expression recognizer using modified ResNet-152," *EAI Endorsed Trans. Internet Things*, vol. 7, no. 28, p. e5, 2022, doi: 10.4108/eetiot.v7i28.685.

[27] A. D. C. Zebua, D. Y. Marbun, F. Thedora, and M. Harahap, "Classification of Lung Cancer with Convolutional Neural Network Method Using ResNet Architecture," *Teknika*, vol. 13, no. 2, pp. 318–323, 2024, doi: 10.34148/teknika.v13i2.906.

[28] M. Selin and K. P. Mathew, "ResNet152: A Deep Learning Approach for Robust Spoof Detection in Speaker Verification Systems," *J. Wirel. Mob. Networks, Ubiquitous Comput. Dependable Appl.*, vol. 15, no. 3, pp. 354–363, 2024, doi: 10.58346/JOWUA.2024.I3.023.

[29] M. Talo, "Convolutional Neural Networks for Multi-class Histopathology Image Classification," 2019, [Online]. Available: http://arxiv.org/abs/1903.10035

[30] M. Zulhusni, C. A. Sari, and E. H. Rachmawanto, "Implementation of DenseNet121 Architecture for Waste Type

Classification," *Adv. Sustain. Sci. Eng. Technol.*, vol. 6, no. 3, p. 02403015, 2024, doi: 10.26877/asset.v6i3.673.
[31] H. Tian *et al.*, "DenseNet model incorporating hybrid attention mechanisms and clinical features for pancreatic cystic tumor classification," *J. Appl. Clin. Med. Phys.*, vol. 25, no. 7, pp. 1–11, 2024, doi: 10.1002/acm2.14380.
[32] P. M. A. Gawande and S. W. Varade, "MDVPB : Design of an Efficient Modified Densenet-161 Model for Advanced Vein Pattern Recognition in Biomedical Systems," vol. 31, no. 8, pp. 692–714, 2024, DOI: https://doi.org/10.52783/cana.v31.1578
[33] B. Alnur, Mulyono, Fitri Amillia, and S. Sutoyo, "JITE (Journal of Informatics andTelecommunication Engineering)," *J. Informatics Telecommun. Eng.*, vol. 7, no. 1, pp. 102–111, 2023, [Online]. Available: https://www.researchgate.net/publication/335117624_Malang_City_Polytechnic_Web_Based_Student_Attendance_Information_System_Telecommunications_Engineering_Study_Program_Using_Fingerprint/fulltext/5d515fe34585153e594ef214/Malang-City-Polytechnic-Web-Based-S
[34] B. Van Calster, L. Wynants, G. S. Collins, J. Y. Verbakel, and E. W. Steyerberg, "ROC curves for clinical prediction models part 3. The ROC plot: a picture that needs a 1000 words," 2020. doi: 10.1016/j.jclinepi.2020.05.037.
[35] J. Li, "Area under the ROC Curve has the most consistent evaluation for binary classification," *PLoS One*, vol. 19, no. 12 December, 2024, doi: 10.1371/journal.pone.0316019.
[36] T. C. F. Polo and H. A. Miot, "Use of roc curves in clinical and experimental studies," 2020. doi: 10.1590/1677-5449.200186.
[37] M. M. Ali, M. S. Islam, M. N. Uddin, and M. A. Uddin, "A conceptual IoT framework based on Anova-F feature selection for chronic kidney disease detection using deep learning approach," *Intell. Med.*, vol. 10, no. July, p. 100170, 2024, doi: https://doi.org/10.1590/1677-5449.200186.
[38] X. Gao, N. Jamil, M. I. Ramli, and S. M. Z. S. Z. Ariffin, "A Comparative Analysis of Combination of CNN-Based Models with Ensemble Learning on Imbalanced Data," *Int. J. Informatics Vis.*, vol. 8, no. 1, pp. 456–464, 2024, doi: 10.62527/joiv.8.1.2194.
[39] N. Hernandez, F. Carrillo-Perez, F. M. Ortuño, I. Rojas, and O. Valenzuela, "Understanding the Impact of Deep Learning Model Parameters on Breast Cancer Histopathological Classification Using ANOVA," *Cancers (Basel).*, vol. 17, no. 9, pp. 1–24, 2025, doi: 10.3390/cancers17091425.
[40] S. Waziry, A. B. Wardak, J. Rasheed, R. M. Shubair, K. Rajab, and A. Shaikh, "Performance comparison of machine learning driven approaches for classification of complex noises in quick response code images," *Heliyon*, 2023, doi: 10.1016/j.heliyon.2023.e15108.
[41] N. K. Naik, M. V. Subbarao, P. K. Sethy, S. K. Behera, and G. R. Panigrahi, "Machine learning with analysis-of-variance-based method for identifying rice varieties," *J. Agric. Food Res.*, vol. 18, no. March, p. 101397, 2024, doi: 10.1016/j.jafr.2024.101397.